Moment Closure Description of Polydisperse, Polykinetic and Evaporating Liquid Sprays

T. F. Leung and C. P. T. Groth
Corresponding author: timf.leung@mail.utoronto.ca

University of Toronto Institute for Aerospace Studies
4925 Dufferin Street, North York, Ontario, Canada, M3H 5T6

Abstract: The description of liquid sprays is commonly modelled using a statistical approach and can be described using a droplet number density function (NDF) which evolves according to the Williams-Boltzmann equation. Approximate solutions to the Williams-Boltzmann equation can be obtained either using Lagrangian particle methods or Eulerian moment closure methods. While Lagrangian methods have been applied to a wide range of sprays in the disperse spray regime, the method can potentially be computationally expensive and require a large number of particles in order to obtain converged statistics. Conversely, moment closure methods operate within an Eulerian framework which can take advantage existing techniques to reduce the computational cost, such as load balancing and mesh adaptation strategies. In addition, an Eulerian framework is consistent with descriptions of the dense spray regime and background carrier phase which simplifies the coupling between the different models. In this study, an extended moment closure model based on the 10-moment anisotropic Gaussian (AG) closure from kinetic theory is presented. Additional size and size-velocity moments are introduced in order to describe the spray polydisperity and droplet size-velocity correlations. Closure is achieved by assuming functional forms of the size-conditioned moments based on entropy maximization and polynomial expressions. The size distribution is modelled using a five-moment maximum entropy distribution which is valid over the entire realizable size moment space and can describe a wide range of different size configurations in practical combustion applications. To deal with numerical robustness issues that can occur at the moment realizability space boundaries, an interpolative approximation for the closing fluxes is proposed. Finally, treatments for relevant spray physics, such as droplet drag and evaporation have been incorporated for realistic applications of large Reynolds and Stokes numbers. Several spray problems are considered to illustrate the predictive capabilities of the moment closure, including a purely evaporating laminar jet using the d^2-evaporation law, a space-homogeneous problem with Stokes drag, a laminar liquid jet in a crossflow with a general drag law, and an atomizing turbulent jet coupled to a dense spray description with two-way coupling to the gaseous carrier phase.

Keywords: Maximum-entropy Moment Closures, Multiphase flows, Spray Modelling, Polydisperse sprays.

1 Introduction

Liquid atomization is ubiquitous in everyday applications and can be found in many engineering systems and devices related to power generation, engines, agriculture and chemical engineering [1]. Of particular interest here is the application of liquid spray atomization to the fuel injection systems of gas turbine engines burning hydrocarbon fuels, where efforts are underway to lower emissions of carbon dioxide (CO_2), mono-nitrogen oxides (NO_X), as well as soot particulate matter. One possible area of improvement in the design of cleaner engines is the fuel injection nozzles. Finer atomization of fuel droplets can promote both better fuel-air mixing and hence cleaner combustion. Crucial to the development of improved fuel injection systems is

the ability to accurately model the spray atomization process using computational fluid dynamic (CFD) simulations. Accurate, affordable, and reliable computational tools are required to explore different design configurations prior to the prototyping process.

The challenge of modelling disperse sprays, which are of primary interest here, is directly related to the multi-phase nature of the problem, as sprays are liquid phase droplets suspended within a gaseous phase carrier flow. The most common spray models are based on an Euler-Lagrange framework wherein the carrier flow is treated as a continuum (Eulerian treatment) while the droplets are modelled as a collection of particles (Lagrangian treatment) whose trajectories are tracked based on Newton's second law. Such a framework can present several computational issues, such as the need for a large number of particles to obtain accurate and converged results. An Euler-Lagrange treatment is also at odds with mesh refinement techniques [2–4] now commonly used in many CFD approaches, as increasing the number of cells in a simulation with a fixed finite number of particles decreases the number of particles per cell, which has the effect of increasing the statistical error of quantities within each cell [5]. It can also introduce errors in cases where the mesh resolution becomes on the order or smaller than the typical droplet size, in which case the droplets can space several computational cells [6]. Furthermore, representing phases as disparate entities works well for one-way coupled flows (wherein the carrier flow affects the disperse phase only), but does not work well two-way coupled flows (wherein the carrier and droplet phases affect each other). Euler-Lagrange-based solutions of the latter often fails to provide grid-independent solutions for inter-phase momentum exchange [7].

An alternative approach is pursued in this study in the form of an Euler-Euler framework, wherein both phases are treated as (Eulerian) continua and an Eulerian-based moment closure method is adopted for the disperse liquid phase. This approach does not require particle tracking and allows for the solution of the carrier gaseous flow and droplets on the same computational mesh. The Euler-Euler treatment is thereby readily amenable to mesh adaptation strategies and provides for a natural two-way coupling between the phases. Furthermore, parallel implementations on multi-processor/multi-core systems are also more straightforward with the Euler-Euler framework, making such approaches potentially more efficient from a computational standpoint. Note that Euler treatments for the disperse phase are however not without their drawbacks. They introduce numerical dissipation that Lagrange disperse phase treatments of do not have. In addition, they require special treatments to handle vacuum regions (i.e., regions with no droplets) and high Stokes number phenomena, such as particle trajectory crossings (PTCs). The associated moment equations can also allow for the occurrence of discontinuous solutions and shock structures which must be properly dealt with when constructing numerical solutions.

For the proposed Euler-Euler treatment, a polydisperse, polykinetic, Eulerian-based model for disperse liquid sprays is developed herein, along with a robust finite-volume method for the numerical solution of the resulting system of hyperbolic moment equations. The polydisperse, polykinetic, moment closure provides approximate solutions to the Williams-Boltzmann equation for disperse sprays and is based on the 10-moment Anisotropic Gaussian (AG) velocity moment closure [8–12] which presents many desirable mathematical properties, such as strict hyperbolicity and moment realizability. Spray droplets of varying sizes can be described by assuming that the velocity moments are conditional functions of a droplet size variable and then transporting additional moments in both size and velocity to describe the polydisperse behaviour. The moment closure is formulated for general drag and evaporation laws for the case of a disperse droplet population moving through a prescribed background gaseous flow. Numerical results are presented for a purely evaporating jet using the d^2-evaporation law, a space-homogeneous problem with Stokes drag, a liquid jet in a crossflow with a general drag law, and a plain orifice atomizing turbulent jet coupled to a dense spray description with two-way coupling to the gaseous carrier phase to demonstrate the abilities of the moment closure method, combined with a robust finite-volume scheme, to capture a range of polydisperse, polykinetic, spray phenomena.

2   Polydisperse, Polykinetic, Moment Closure for Dilute Sprays

2.1   Williams-Boltzmann Kinetic Equation

The Williams-Boltzmann kinetic equation [13] governs the time-evolution and transport of the number density function (NDF), $\mathcal{F}(t, x_i, v_i, S)$, for disperse spray droplets through a seven dimensional phase space,

(x_i, v_i, S), and in time, t, and can be written as

$$\frac{\partial \mathcal{F}}{\partial t} + \frac{\partial}{\partial x_i}\left(v_i \mathcal{F}\right) + \frac{\partial}{\partial v_i}\left(a_i \mathcal{F}\right) + R_S \frac{\partial \mathcal{F}}{\partial S} = Q + \Gamma, \tag{1}$$

where v_i is the droplet velocity vector, S is the droplet surface area, x_i is the position vector in physical space, R_S is the evaporation rate (strictly negative), a_i is the acceleration due to external forces, Q is the rate of formation associated with new droplets, and Γ is associated with inter-droplet collisional processes. In this study, the sprays are taken to be dilute and coalescence, breakup and collisions are neglected. The focus here is placed on treatments for drag and evaporation.

2.2 20-Moment Anisotropic Gaussian (AG) Moment Closure

Direct solution of the Williams-Boltzmann equation is prohibitively expensive due to the high dimensionality of the associated phase space. However, approximate solutions of the Williams-Boltzmann equation can be obtained by deriving a set of transport equations for the moments of the droplet NDF which are relevant, since the quantities of interest for typical engineering applications are macroscopic quantities such as the mean droplet size and velocity, and then formulating a closure for the moment system. The transport equations can be obtained by multiplying the NDF by a combined size-velocity weight, $\boldsymbol{\mathcal{W}}(v_i, S)$, and integrating over phase space, which is represented in this manuscript by the angle-bracket notation, $\langle . \rangle$. Size moments related to the geometrical parameters of the spray can be obtained for $\boldsymbol{\mathcal{W}}(v_i, S) = S^k$ and are given by

$$\mathcal{M}_k = \langle S^{\frac{k}{2}} \mathcal{F} \rangle = \int_0^{S_{max}} \iiint_\infty S^{\frac{k}{2}} \mathcal{F} \, \mathrm{d}^3 v \mathrm{d}S. \tag{2}$$

Similarly, velocity moments related to the weighted mean droplet velocity can be obtained for $\boldsymbol{\mathcal{W}}(v_i, S) = S^k v_i$. For example, the number density weighted mean droplet velocity, $U_i^{(0)}$, can be obtained from

$$\mathcal{M}_0 U_i^{(0)} = \langle S^0 v_i \mathcal{F} \rangle = \int_0^{S_{max}} \iiint_\infty v_i \mathcal{F} \, \mathrm{d}^3 v \mathrm{d}S. \tag{3}$$

The polydisperse, polykinetic, moment closure proposed herein is an extension of the 10-moment AG maximum-entropy velocity closure from kinetic theory, essentially a monodisperse description, that has been extended to include dependency of the NDF on droplet size. Similar to the approach adopted by Wang [14], the 20-Moment AG polydisperse closure is derived by considering a vector of combined size-velocity weights, $\boldsymbol{\mathcal{W}}(v_i, S)$, given by

$$\boldsymbol{\mathcal{W}}(v_i, S) = \left[1, S^{\frac{1}{2}}, S, S^{\frac{3}{2}}, S^2, v_i, S^{\frac{1}{2}} v_i, S v_i, v_i v_j\right]^T, \tag{4}$$

which define a finite set of size and velocity moments, $\mathbf{M}$, given by

$$\mathbf{M} = \left[\mathcal{M}_0, \mathcal{M}_1, \mathcal{M}_2, \mathcal{M}_3, \mathcal{M}_4, \mathcal{M}_0 U_i^{(0)}, \mathcal{M}_1 U_i^{(1)}, \mathcal{M}_2 U_i^{(2)}, \mathcal{M}_0 \left(U_i^{(0)} U_j^{(0)} + \Sigma_{ij}^{(0)}\right)\right]^T. \tag{5}$$

The corresponding system of moment equations for these macroscopic size and velocity moments is then

given by

$$\frac{\partial}{\partial t}\left(\mathcal{M}_0\right) + \frac{\partial}{\partial x_i}\left(\mathcal{M}_0 U_i^{(0)}\right) = A^{(0)}$$

$$\frac{\partial}{\partial t}\left(\mathcal{M}_1\right) + \frac{\partial}{\partial x_i}\left(\mathcal{M}_1 U_i^{(1)}\right) = A^{(1)}$$

$$\frac{\partial}{\partial t}\left(\mathcal{M}_2\right) + \frac{\partial}{\partial x_i}\left(\mathcal{M}_2 U_i^{(2)}\right) = A^{(2)}$$

$$\frac{\partial}{\partial t}\left(\mathcal{M}_3\right) + \frac{\partial}{\partial x_i}\left(\mathcal{M}_3\, U_i^{(3)}\right) = A^{(3)}$$

$$\frac{\partial}{\partial t}\left(\mathcal{M}_4\right) + \frac{\partial}{\partial x_i}\left(\mathcal{M}_4\, U_i^{(4)}\right) = A^{(4)}$$

$$\frac{\partial}{\partial t}\left(\mathcal{M}_0 U_i^{(0)}\right) + \frac{\partial}{\partial x_i}\left[\mathcal{M}_0\left(U_i^{(0)}U_j^{(0)} + \Sigma_{ij}^{(0)}\right)\right] = B_i^{(0)}$$

$$\frac{\partial}{\partial t}\left(\mathcal{M}_1 U_i^{(1)}\right) + \frac{\partial}{\partial x_i}\left[\mathcal{M}_1\left(U_i^{(1)}U_j^{(1)} + \Sigma_{ij}^{(1)}\right)\right] = B_i^{(1)}$$

$$\frac{\partial}{\partial t}\left(\mathcal{M}_2 U_i^{(2)}\right) + \frac{\partial}{\partial x_i}\left[\mathcal{M}_2\left(U_i^{(2)}U_j^{(2)} + \Sigma_{ij}^{(2)}\right)\right] = B_i^{(2)}$$

$$\frac{\partial}{\partial t}\left[\mathcal{M}_0\left(U_i^{(0)}U_j^{(0)} + \Sigma_{ij}^{(0)}\right)\right] + \frac{\partial}{\partial x_i}\left[\mathcal{M}_0\left(U_i^{(0)}U_j^{(0)}U_k^{(0)} + U_i^{(0)}\Sigma_{jk}^{(0)} + U_j^{(0)}\Sigma_{ik}^{(0)} + U_k^{(0)}\Sigma_{ij}^{(0)} + Q_{ijk}^{(0)}\right)\right] = C_{ij}^{(0)}.$$
(6)

The first five equations are associated with mass conservation and describe the evolution of mean geometrical quantities of the spray, such as droplet length, surface area, volume, and hypervolume, respectively. The next three equations represent momentum conservation for the polydisperse spray and describe the evolution of mean droplet velocity weighted by the number density, length, and surface area, respectively. Finally, the last equation is akin to energy conversation equation for the spray and represents the total kinetic energy of the spray droplets.

Unfortunately, the highlighted fluxes in Eq. (6) above are unclosed and an approach to formal closure is required. Various source terms may also require closure, depending on the modelled spray physics. Closure of the system is obtained here by imposing additional assumptions on the form of the NDF. In the proposed AG-based closure, the NDF, $\mathcal{F}(t, x_i, v_i, S)$, is taken to have the form

$$\mathcal{F}(t, x_i, v_i, S) = \frac{n(t, x_i, S)}{(2\pi)^{3/2}\sqrt{\det \sigma(t, x_i, S)}} \exp\left\{-\frac{\sigma_{ij}(t, x_i, S)^{-1}}{2}\left[v_i - u_i(t, x_i, S)\right]\left[v_j - u_j(t, x_i, S)\right]\right\}, \quad (7)$$

where $n(S)$, $u_i(S)$ and $\sigma_{ij}(S)$ are the size-conditioned number density, mean velocity and variance, respectively, which depend directly on the droplet size parameter, S. Functional forms of these size-conditioned moments are required to complete the closure and are outlined in the sections to follow.

2.3 Maximum Entropy Closure in Size Space

The size-conditioned number density, $n(S)$, is approximated here via the maximum-entropy distribution, which has several desirable properties: it is the most probable distribution based on the available information [15,16] and is able to represent every possible configuration within the moment realizablity space [17]. The maximum-entropy solution for $n(S)$ is derived in terms of the droplet probability density function (PDF), $f(s)$, where s is the normalized droplet size defined for the finite interval $s \in [0, 1]$. This PDF, $f(s)$, is taken to be the solution that maximizes the Shannon entropy subject to the five purely size moment constraints given and is given by

$$\mathcal{H}[(s)] = -\int_0^1 f(s)\ln f(s)ds, \quad \boldsymbol{m} = \int_0^1 \boldsymbol{x}(s)f(s)ds, \quad (8)$$

where $\mathcal{H}$ is the Shannon entropy, $\boldsymbol{m}$ is the vector of normalized size moments and $\boldsymbol{x}(s)$ is the monomial basis vector given by $\boldsymbol{x}(s) = [1, s^{\frac{1}{2}}, s, s^{\frac{3}{2}}, s^2]^T$. The maximization of the entropy, $\mathcal{H}$, subject to the moment

4

constraints, $\boldsymbol{m}$, can then be obtained numerically via Lagrange's method combined with a damped Newton iterative method [18–20].

2.4   Size-Conditioned Mean Velocity and Variance of Velocity

Having defined $n(S)$, the size-conditioned velocity, $u_i(S)$, is then modelled as a polynomial in S given by

$$u_i(S) = a_i + b_i S^{\frac{1}{2}} + c_i S, \tag{9}$$

where a_i, b_i and c_i are the polynomial closure coefficients. Such an approximation has several advantages: the coefficients can be obtained efficiently by solving a linear system, the distribution is able to represent every possible configuration within the moment realizability space and the distribution is non-monotonic and therefore capable of describing velocity reversal in an oscillating turbulent flow [17]. In previous studies [17, 21], the constant a_i is expressed directly as a function of the gaseous carrier phase velocity. However, this condition is not imposed in the current model since it can cause issues when the Stokes number is very large or the carrier phase is absent (i.e. particles in a vacuum with no background gas).

Finally, in the present work, the velocity variance, $\sigma_{ij}(S)$, is assumed to be constant with size, resulting in a so-called partially-polydisperse closure [14]. The full implications of this simplifying assumption remain to be explored and such an assumption may be relaxed in future follow-on research.

2.5   Closure of Moment Equations

Based on the assumptions outlined in the previous sections, the unclosed fluxes appearing in Eq. (6) above can be then expressed as follows:

$$U_i^{(3)} = a_i + b_i \frac{m_4}{m_3} + c_i \frac{m_5}{m_3}, \tag{10}$$

$$U_i^{(4)} = a_i + b_i \frac{m_5}{m_4} + c_i \frac{m_6}{m_4}, \tag{11}$$

$$\Sigma_{ij}^{(1)} = b_i b_j \left[\frac{m_3}{m_1} - \left(\frac{m_2}{m_1} \right)^2 \right] + c_i c_j \left[\frac{m_5}{m_1} - \left(\frac{m_3}{m_1} \right)^2 \right] + (b_i c_j + b_j c_i) \left[\frac{m_4}{m_1} - \frac{m_2 m_3}{m_1^2} \right], \tag{12}$$

$$\Sigma_{ij}^{(2)} = b_i b_j \left[\frac{m_4}{m_2} - \left(\frac{m_3}{m_2} \right)^2 \right] + c_i c_j \left[\frac{m_6}{m_2} - \left(\frac{m_4}{m_2} \right)^2 \right] + (b_i c_j + b_j c_i) \left[\frac{m_5}{m_2} - \frac{m_3 m_4}{m_2^2} \right], \tag{13}$$

$$Q_{ijk}^{(0)} = (a_i b_j b_k + a_j b_i b_k + a_k b_i b_j) \left[m_2 - m_1^2 \right] + (a_i b_j c_k + a_i b_k c_j + a_j b_i c_k + a_j b_k c_i + a_k b_i c_j + a_k b_j c_i) \left[m_3 - m_1 m_2 \right]$$

$$+ (b_i b_j b_k) \left[m_3 - m_1^3 \right] + (a_i c_j c_k + a_j c_i c_k + a_k c_i c_j) \left[m_4 - m_2^2 \right] + (c_i b_j b_k + c_j b_i b_k + c_k b_i b_j) \left[m_4 - m_1^2 m_2 \right]$$

$$+ (b_i c_j c_k + b_j c_i c_k + b_k c_i c_j) \left[m_5 - m_1 m_2^2 \right] + (c_i c_j c_k) \left[m_6 - m_2^3 \right]$$

$$+ (a_i + b_i m_1 + c_i m_2) \left[\sigma_{jk} - \Sigma_{jk}^{(0)} \right] + (a_j + b_j m_1 + c_j m_2) \left[\sigma_{ik} - \Sigma_{ik}^{(0)} \right] + (a_k + b_k m_1 + c_k m_2) \left[\sigma_{ij} - \Sigma_{ij}^{(0)} \right], \tag{14}$$

where the highlighted terms, m_k, are higher-order size moments which can be obtained directly via integration using the maximum-entropy size distribution, $f(s)$. It should however be noted that the solution of the maximum-entropy problem requires the iterative solution of a non-linear system of equations and can therefore be computationally expensive. As an alternative, these terms can be approximated using an interpolative procedure based on pre-computed solutions of the maximum-entropy problem. Such an approach is considered here and discussed in a later section.

2.6   Treatment of Moment Closure Near the Realizability Space Boundaries

A key issue associated with moment closure is realizability [22]. Moment realizability is concerned with ensuring that the predicted moments of the closure are physically realizable and can be associated with

(a) Size-conditioned Droplet PDF

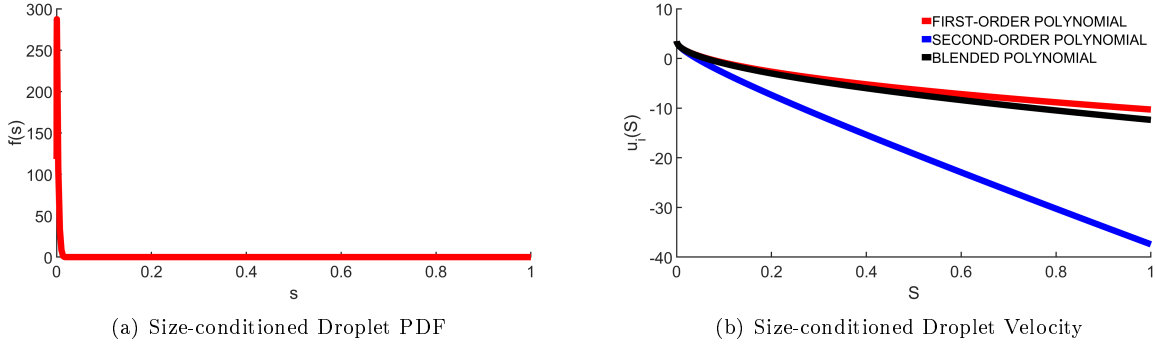(b) Size-conditioned Droplet Velocity

Figure 1: Size-conditioned droplet PDF and velocity near the moment realizability space boundary.

a strictly positive NDF. In the case of the solution of the maximum-entropy problem defining the size-conditioned number density, $n(S)$, moment realizability places constrints or conditions on the values of the pure size moments, m_k. When the vector of size moments for the maximum-entropy solution approaches the boundaries of realizability space defined by the contraints, the size distribution approaches a linear combination of delta-functions, as shown in Figure 1(a), causing numerical issues which can impact the numerical solution of the maximum-entropy problem as well as the accurate treatment of the size-conditioned velocity, $u_i(S)$.

First, at the realizability space boundaries, the constraints on the maximum entropy problem are almost linearly dependant and the Hessian used in the Newton method can be badly conditioned. The conditioning can be improved by transforming the original set of constraint equations to an orthonormal set using a Cholesky factorization procedure [20]. In addition, the numerical integration of the moments used in the constraint equations are inaccurate when the size distribution is very peaked. One approach for improving the accuracy is to use adaptive quadrature [17]; however, it was found that this approach had a slower convergence rate and was prone to stall. Instead, it was found to be more efficient to use a fixed number of quadrature points and if the solver is unable to converge within a reasonable number of iterations, the solver is reset and the number of quadrature points used for the integration is doubled. In the cases tested, it was found that a 65-point Clenshaw-Curtis quadrature rule was sufficient for obtaining a converged maximum entropy solution to within an absolute error of 10^{-9}.

Another potential issue that can arise is associated with the modelling of the size-conditioned velocity, $u_i(S)$, which is a function of the first-order velocity moments given by the following

$$\langle S^k v_i \mathcal{F} \rangle = \int_0^{S_{max}} S^k n(S) u_i(S) \mathrm{d}S. \tag{15}$$

In the equation above, the first-order velocity moments are weighted by $n(S)$, which is close to singular near the realizability space boundaries. For values of S where $n(S)$ is close to zero, $u_i(S)$ can essentially take on any value since the second-order polynomial construction of $u_i(S)$ is unbounded. Consequently, very large and unreliable values of $u_i(S)$ can be obtained when $n(S)$ is very small, as can be seen in Figure 1(b), where the magnitude of $u_i(S = 1)$ is very large relative to the mean velocity, where $U_x = 2.85 \ m/s$, and this can potentially affect the modelling accuracy since the size-conditioned velocity is used to compute the closing fluxes. The issue can be alleviated by introducing a relaxation parameter, r, that modifies $u_i(S)$ such that it approaches a first-order polynomial as $r = 0$, with the modified polynomial coefficients defined as

$$\begin{aligned}
a_i &= (1-r)a_i^{p_2} + r a_i^{p_4}, \\
b_i &= (1-r)b_i^{p_2} + r b_i^{p_4}, \\
c_i &= r c_i^{p_4}.
\end{aligned} \tag{16}$$

6

The parameter r acts as a blending function which is bounded between 0 and 1 and is defined as

$$r = \begin{cases} \frac{\tilde{r}}{r_0} & \text{if } \tilde{r} \le r_0 \\ 1 & \text{otherwise} \end{cases} , \quad \tilde{r} = p_1 p_2 p_3 p_4 (1 - p_1)(1 - p_2)(1 - p_3)(1 - p_4) , \tag{17}$$

where r_0 is a user-defined constant and $\tilde{r}$ is a function that approaches zero as the moment vector approaches the realizability space boundaries. The relaxation or blending parameter, r, allows for a relatively smooth transition between a first and second-order polynomial reconstruction of $u_i(S)$ so that the closing fluxes are relatively smooth functions of the known size and velocity moment vectors. Finally, the polynomial coefficients in Eq. (16) are obtained by solving the following linear systems

$$\begin{aligned} A^{p_2} \boldsymbol{x}^{p_2} &= \boldsymbol{b}^{p_2} , \\ A^{p_4} \boldsymbol{x}^{p_4} &= \boldsymbol{b}^{p_4} , \end{aligned} \tag{18}$$

where

$$A^{p_2} = \begin{bmatrix} \langle S^0 \mathcal{F} \rangle & \langle S^{\frac{1}{2}} \mathcal{F} \rangle \\ \langle S^{\frac{1}{2}} \mathcal{F} \rangle & \langle S^1 \mathcal{F} \rangle \end{bmatrix}, \boldsymbol{x}^{p_2} = \begin{bmatrix} a_i^{p_2} \\ b_i^{p_2} \end{bmatrix}, \boldsymbol{b}^{p_2} = \begin{bmatrix} \langle S^0 \mathcal{F} \rangle U_i^{(0)} \\ \langle S^{\frac{1}{2}} \mathcal{F} \rangle U_i^{(1)} \end{bmatrix} , \tag{19}$$

and

$$A^{p_4} = \begin{bmatrix} \langle S^0 \mathcal{F} \rangle & \langle S^{\frac{1}{2}} \mathcal{F} \rangle & \langle S^1 \mathcal{F} \rangle \\ \langle S^{\frac{1}{2}} \mathcal{F} \rangle & \langle S^1 \mathcal{F} \rangle & \langle S^{\frac{3}{2}} \mathcal{F} \rangle \\ \langle S^1 \mathcal{F} \rangle & \langle S^{\frac{3}{2}} \mathcal{F} \rangle & \langle S^2 \mathcal{F} \rangle \end{bmatrix}, \boldsymbol{x}^{p_4} = \begin{bmatrix} a_i^{p_4} \\ b_i^{p_4} \\ c_i^{p_4} \end{bmatrix}, \boldsymbol{b}^{p_4} = \begin{bmatrix} \langle S^0 \mathcal{F} \rangle U_i^{(0)} \\ \langle S^{\frac{1}{2}} \mathcal{F} \rangle U_i^{(1)} \\ \langle S^1 \mathcal{F} \rangle U_i^{(2)} \end{bmatrix} . \tag{20}$$

2.7 Interpolative Closure for the Fluxes

To improve the efficiency and robustness of the proposed 20-moment AG closure, an interpolative approach is also proposed here where the high-order moments, m_k, are approximated using spline functions. The higher-order moments can be expressed as a function of the lower-order canonical moments, which correspond to moments normalized by the realizability space boundaries and are defined as

$$p_k = \frac{m_k - m_k^-}{m_k^+ - m_k^-} , \tag{21}$$

where m_k^- and m_k^+ are respectively the minimum and maximum realizable values for the kth moment. The interpolative-based approximations for the size moments are obtained by fitting spline basis functions to the higher-order moments of the maximum-entropy distribution with the following form

$$\tilde{m}_k^{ME}(p_1, p_2, p_3, p_4) = \sum_{a_0 = -3}^{N_a - 1} \sum_{b_0 = -3}^{N_b - 1} \sum_{c_0 = -3}^{N_c - 1} \sum_{d_0 = -3}^{N_d - 1} \tau_{k,abcd} N_a(p_1) N_b(p_2) N_c(p_3) N_d(p_4) , \tag{22}$$

where τ are the control points and $N_i(p_k)$ are the basis functions. Near the boundaries of realizability space where p_2 and p_4 approach zero, the variation of the high-order moments with respect to the canonical moments is more significant and more data points are used for the approximation.

2.8 Treatment of Drag and Evaporation Source Terms

Important physical processes associated with spray transport are incorporated in the moment closure through the imposition of source terms and, in the present study, drag and evaporation are considered. The velocity and size dependent droplet acceleration, a_i, due to the drag force is taken to have the form

$$a_i(v_i, S) = \frac{18\pi\mu_g}{\rho_l S}[u_{g,i} - v_i]\frac{Re(v_i, S)}{24}C_D(Re), \tag{23}$$

where μ_g is the viscosity of the carrier phase, ρ_l is the droplet density, $u_{g,i}$ is the velocity of the carrier phase, Re is the Reynolds number of the droplet and C_D is the droplet drag coefficient. The drag coefficient
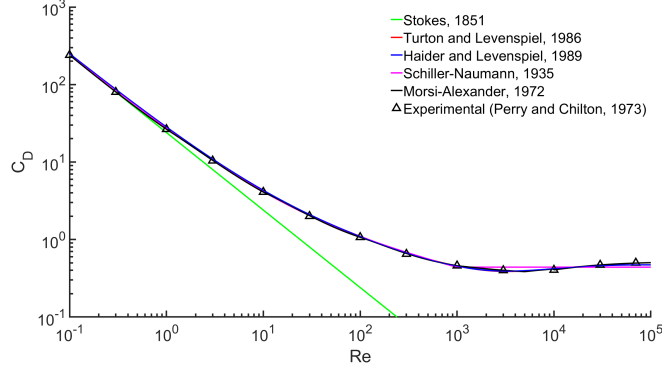
Figure 2: Comparison of various empirical drag correlations with experimental results.

is a function of the Reynolds number, as illustrated in Figure 2, where different empirical correlations are compared to the drag coefficient obtained from experiment. There are essentially three regions in the curve: a region for $Re \sim 0.1$ (also known as Stokes flow) where the drag coefficient is given by $C_D = \frac{24}{Re}$, a region for $Re \sim 10^3$ where the drag coefficient is approximately constant with a value of $C_D = 0.4$ and an intermediate region where the drag coefficient is a complicated function of Re. For very small Reynolds numbers, the Stokes correlation is a good approximation of the drag force but can significantly under-predict the drag force for larger Reynolds numbers. The other correlations shown all have relatively good agreement with the experimental data over the full range of Reynolds number. In this study, the Haider-Levenspiel empirical correlation [23] is used to specify C_D since it is a smooth function function of the Reynolds number, unlike the Schiller-Naumann and Morsi-Alexander correlations which have discontinuous derivatives with respect to Re. The drag source term vector can then be obtained by integrating the following expression over phase space

$$S_{drag} = \left\langle \boldsymbol{\mathcal{W}}(v_i, S) \frac{\partial}{\partial v_i} (a_i \mathcal{F}) \right\rangle, \tag{24}$$

where the Curtis-Clenshaw and Gauss-Hermite quadrature rules are used for integration over size and velocity space, respectively.

For treatment of droplet evaporation, which affects the evolution of the size moments, the system of equations is solved using a fractional step or splitting method in order to preserve realizability of the moment vector. A first-order fractional step approach is adopted here, where the original kinetic equation is decomposed into the following two stages given by

$$\frac{\partial \mathcal{F}}{\partial t} + \frac{\partial}{\partial x_i} (v_i \mathcal{F}) = -\frac{\partial}{\partial v_i} (a_i \mathcal{F}), \tag{25}$$

$$\frac{\partial \mathcal{F}}{\partial t} = -R_S \frac{\partial \mathcal{F}}{\partial S}. \tag{26}$$

For the d^2-evaporation law considered here, then R_S is then constant and the exact solution of Eq. (26) is given by

$$\mathcal{F}(t, S) = \mathcal{F}(S - R_S t), \tag{27}$$

which represents the translation of the NDF in size space. The conserved moments at the new time step are obtained by integrating the product of Eq. (27) with the vector of size-velocity weights, $\boldsymbol{\mathcal{W}}(v_i, S)$, and are guaranteed to be realizable since they are obtained from the integration of a non-negative NDF.

8

3 Eulerian-Eulerian Spray Atomization Model (EESA): Coupling of Σ-Y 20-Moment Closure

As part of the current effort, the proposed 20-moment AG closure has also been coupled to the Σ-Y model, providing a complete approximate description of both the dense spray atomization processes and subsequent droplet transport associated with polydisperse sprays. In the dense spray regime, the spray is not yet fully atomized into droplets and consists of an intact liquid core and larger ligaments of the liquid spray which cannot be accurately described by a statistical resprentation in terms of a droplet NDF. The Σ-Y model is a previously proposed quasi-multiphase mixture model with two additional equations which tracks the liquid volume fraction and interface area density [6,24,25] and can be used here to represent the dense phase. The primary atomization processes in this case are modelled using empirically derived source terms. When the spray is considered to be sufficiently disperse (based on the local values of the liquid volume fraction and surface density), the disperse spray content of the AG moment closure is introduced via source term transfer in both the Σ-Y and moment closure descriptions. In addition, the Σ-Y model and AG moment closure is two-way coupled to the background gaseous carrier phase via additional momentum source terms and the full Navier-Stokes equations for the carrier phase are solved along with the transport equations of the Σ-Y model and AG moment closure using a segregated solution procedure. The complete description of the dense and disperse spray processes is referred to here as the Eulerian-Eulerian spray atomization model (EESA).

Details regarding the implementation of the Σ-Y model used in this work will now be discussed. Similar to RANS-based turbulence models, the Σ-Y model describes the large scale processes for turbulent spray atomization while the subgrid features are modelled using diffusion and source terms. The transport equations for the liquid mass fraction, $\tilde{Y}$, and mass-weighted surface density, $\tilde{\Omega}$, are given by

$$\frac{\partial}{\partial t}\left(\bar{\rho}\tilde{Y}\right) + \frac{\partial}{\partial x_i}\left(\bar{\rho}\tilde{u}_i\tilde{Y}\right) = -\frac{\partial}{\partial x_i}\left(\widetilde{\bar{\rho}u_i''Y''}\right) + S_{Y,trans}\,, \tag{28}$$

$$\frac{\partial}{\partial t}\left(\bar{\rho}\tilde{\Omega}\right) + \frac{\partial}{\partial x_i}\left(\bar{\rho}\tilde{u}_i\tilde{\Omega}\right) = \frac{\partial}{\partial x_i}\left[\left(\frac{\mu_t}{Sc_t}\right)\frac{\partial\tilde{\Omega}}{\partial x_i}\right] + \Psi(S_{init}+S_{primary}) + (1-\Psi)(S_{coll}+S_{2ndBU}) + S_{evap} + S_{\Omega,trans}\,, \tag{29}$$

where $\widetilde{\bar{\rho}u_i''Y''}$ is the turbulent liquid flux and is modelled using a gradient-based closure [24] given by

$$\widetilde{\bar{\rho}u_i''Y''} \approx -\frac{\mu_t}{Sc_t}\frac{\partial\tilde{Y}}{\partial x_i}\,. \tag{30}$$

The source terms that appear on the RHS of equation (29) correspond to different atomization processes including: primary breakup, collision/coalescence, secondary breakup and evaporation. Following the modelling approach of Lebas *et. al* [25], they are modelled as relaxation processes of the following general form

$$S = \alpha\frac{\bar{\rho}\tilde{\Omega}}{\tau}\left(1 - \frac{\tilde{\Omega}}{\tilde{\Omega}^*}\right)\,, \tag{31}$$

where α is an empirical constant, τ is the characteristic time scale and $\tilde{\Omega}^*$ is the equilibrium surface density.

The model transition between the Σ-Y model and the 20-moment AG closure occurs when the liquid volume fraction is below some critical value, at which point the spray is considered to be disperse and the transition source terms, $S_{Y,trans}$ and $S_{\Omega,trans}$ in equations (28) and (29) become active. Although the activation criteria is currently discontinuous with respect to the liquid volume fraction, smooth functions will be investigated in the future. Below the critical value, the transition source terms vary linearly with respect to the liquid volume fraction and remain active until the liquid volume fraction is zero.

For the initialization process of the 20-moment closure, some additional assumptions about the droplet NDF are necessary since the Σ-Y model does not include a complete description of the droplet NDF. During the initialization process, it is assumed that the droplet size and velocity are uncorrelated. In addition, the size-conditioned number density is assumed to be log-normal and the SMD is assumed to be a function of the arithmetic mean diameter. Finally, it is assumed that the velocity distribution is Gaussian and the velocity variance is related to the turbulent kinetic energy [26].

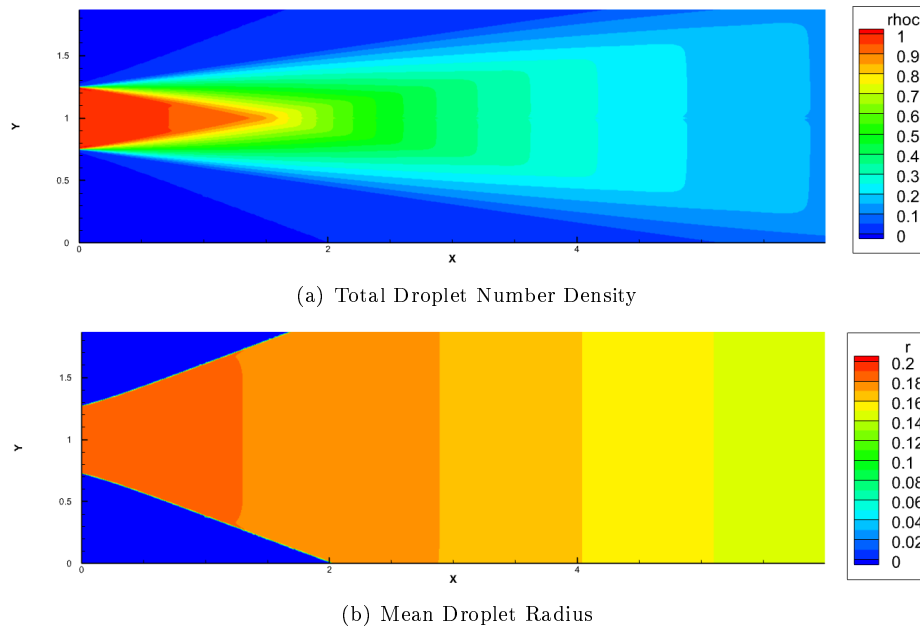(a) Total Droplet Number Density

(b) Mean Droplet Radius

Figure 3: Numerical predictions of purely evaporating jet showing the predicted distributions of the total droplet number density and mean droplet diameter.

4   Numerical Solution Method

The hyperbolic moment equations of the proposed 20-moment AG closure admit discontinuous solutions and shock structures (such features are common as the velocity variance of the droplets can be small and hence the droplet flow is "supersonic") and are therefore solved here using a Godunov-type finite-volume method with piecewise limited linear reconstruction, Venkatakrishnan slope limiter [27], HLL flux function [28] and a two-step second-order accurate strong stability preserving (SSP) Runge-Kutta [29] time-marching scheme. Strang splitting is used for the treatment of the evaporative source term, which is strongly stable and second-order accurate in time. The solution for the carrier or background gas is fully specified and assumed to be unaffected by the spray solution for the first three cases considered in this study. For the final case, the spray solution is two-way coupled to the carrier phase which is solved using ANSYS FLUENT within a second-order finite-volume framework using the pressure-based solver and coupled solution algorithm, where the continuity and momentum equations are solved simultaneously.

5   Numerical Results

5.1   Purely Evaporating Laminar Jet

In the first example test case, a jet of droplets is injected into quiescent air. The problem is solved on a uniform planar mesh consisting of 2,000 cells along the x-axis, 400 cells along the y-axis and 100 cells across the jet. The boundary conditions for the droplet jet at the inlet are: $n(S) = 1.0$ particles/m^3, $\Sigma_{yy} = 1.0$ m^2/s^2 and $U_x = 10$ m/s. Evaporation is modelled using the d^2-evaporation law with $R_S = -0.7$ and it is assumed that there is no drag between the droplets and background gas. As the jet travels downstream, the total number density and mean droplet radius decrease because the droplets are evaporating and mixing with the background carrier phase and the jet spreads out in the y-direction due to the velocity variance specified at the inlet, as can be seen in Figure 3(a) and 3(b), respectively. In Figure 4, the size-conditioned number density, $n(S)$, at different locations along the centerline is shown, confirming that the number density and droplet radius are decreasing as the droplets evaporate.
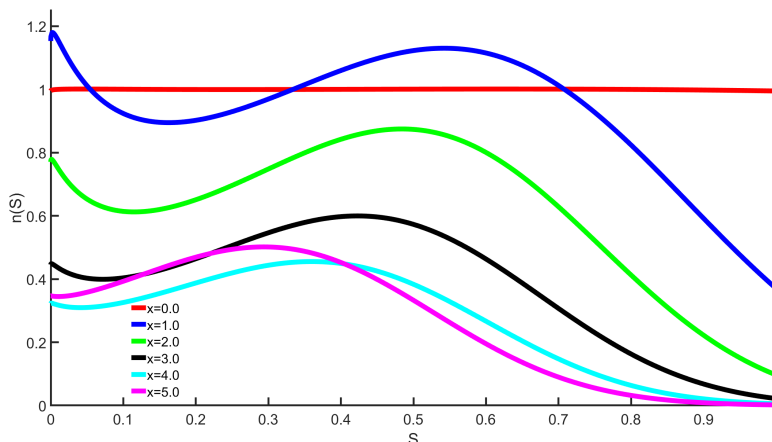
10

Figure 4: Numerical predictions of purely evaporating jet showing the size-conditioned number density, $n(S)$, at different stations along the centerline of the jet.
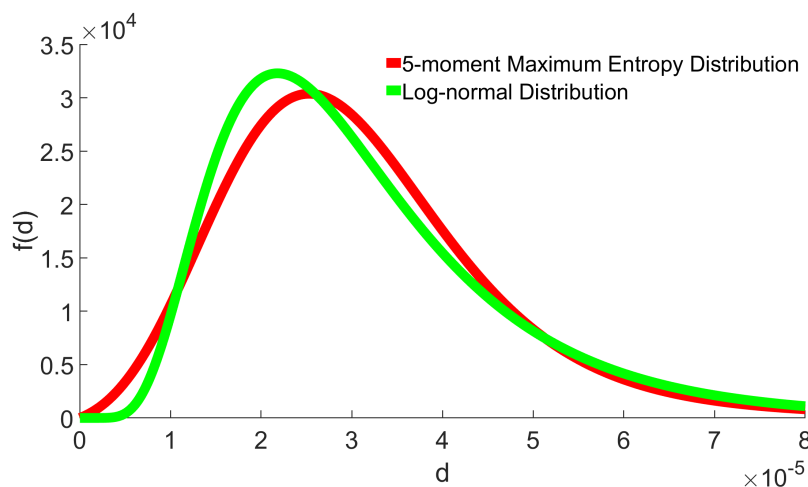

Figure 5: Initial size-conditioned PDF corresponding to the 5-moment maximum entropy closure (red) and log-normal distribution (green) for space homogeneous problem with Stokes drag.

5.2 Space-Homogeneous Problem with Stokes Drag

The second test case is a space-homogeneous problem in physical space in which polydisperse droplets with an initial prescribed velocity are relaxed to the background gas velocity field due to the effects of Stokes drag. The velocity field of the background gas is at rest and the particles have an initial velocity of velocity of $U_x = 5$ m/s, a velocity variance of $\Sigma_{xx} = 1.0$ m^2/s^2, and a size-velocity covariance of $\Sigma_{xd} = 0.0$ m^2/s. The initial size-conditioned PDF is a five-moment maximum entropy distribution where the first five moments are identical to that of a log-normal distribution with $\bar{d} = 3.173 \times 10^{-5}$ m and $\Sigma_{dd} = 2.86 \times 10^{-10}$ m^2, as depicted in Figure 5. As there is no spatial variation in the problem, the evolution of the droplet NDF is fully described by the drag source term and an exact analytic solution can be obtained for this problem [30], which will be used as a benchmark solution to assess the accuracy of the proposed 20-moment AG closure model. In addition, since there is no evaporation, the shape of the size-conditioned PDF does not change in this problem.

First, the NDF obtained from the exact solution is compared to the 20-moment AG closure at three different times shown in Figure 6. From the exact solution, it can be seen that the smaller droplets respond

(a) Exact NDF at $t = 0.0$ s

(b) 20-moment AG closure at $t = 0.0$ s

(c) Exact NDF at $t = 0.61$ s

(d) 20-moment AG closure at $t = 0.61$ s

(e) Exact NDF at $t = 3.03$ s
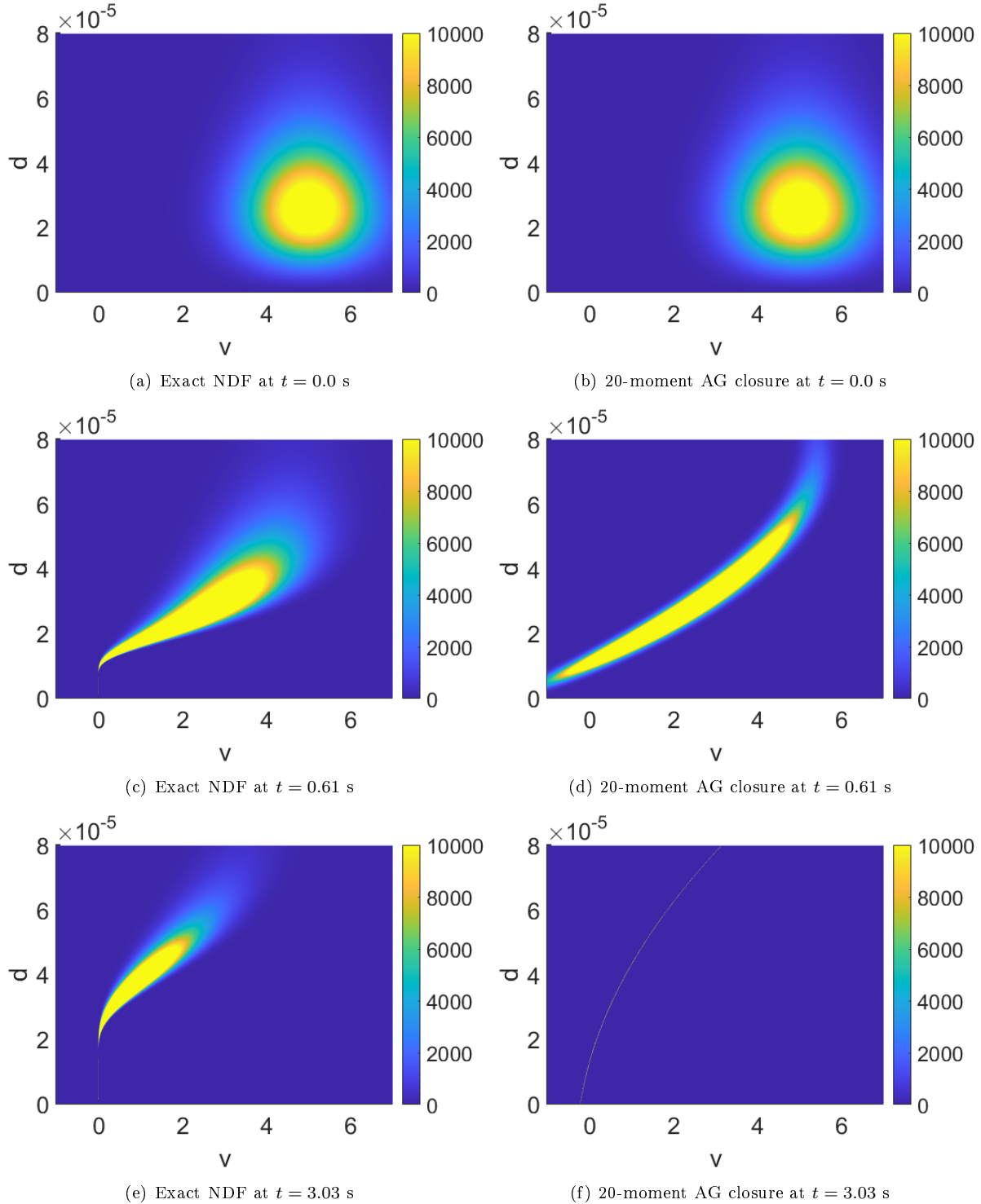
(f) 20-moment AG closure at $t = 3.03$ s

Figure 6: Droplet NDF for the space-homogeneous problem with Stokes drag shown at different instances in time. The exact NDF corresponding to the reference analytical solution is shown on the left and the predictions of the 20-moment AG closure are shown on the right.

more quickly to the drag force and relax to the background gas velocity, where the velocity of the smallest droplets are monokinetic at $v = 0 \ m/s$. The 20-moment AG closure is able to capture the general shape of
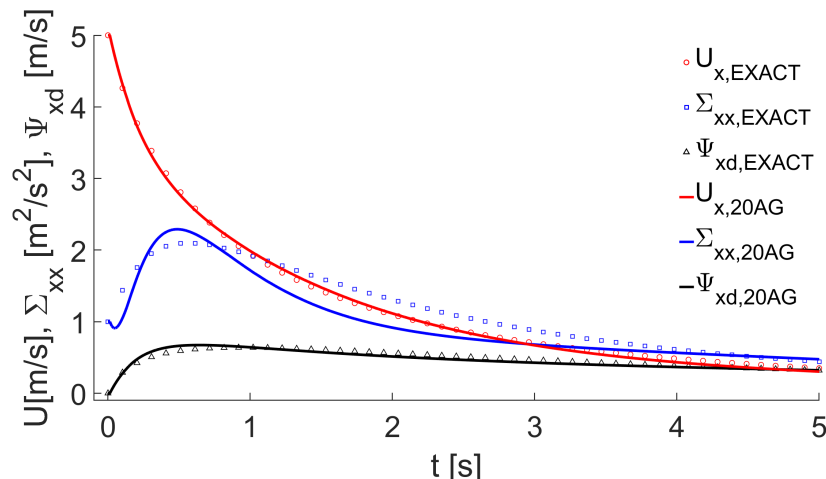
Figure 7: Comparison of the primitive variables between the reference exact solution and the predictions of the 20-moment AG closure for the space-homogeneous problem with Stokes drag.

the NDF, as can be seen in Figures 6(d) and 6(f), although there is a slight overshoot in the velocity of the smallest droplets in Figure 6(f). Nonetheless, it can be seen that the transient behaviour of the proposed model agrees well with that of the exact solution.

Next, the evolution of the primitive variables is compared between the exact solution and the 20-moment AG closure in Figure 7, where the mean velocity, U_x, velocity variance, Σ_{xx}, and size-velocity covariance, Σ_{xd} are compared. It can be seen that the behaviour of U_x and Σ_{xd} agree well with the exact solution, while the initial peak of Σ_{xx} is over-predicted and then subsequently under-predicted compared to the exact solution. The source of the modelling error is likely due to the fact that the size-conditioned velocity of the small droplets are independent of size (since they have relaxed to the carrier phase velocity) while the velocity of the large droplets are still strongly dependant on size, as can be seen in Figures 6(c) and 6(e). This type of behaviour cannot be replicated using a polynomial model for the size-conditioned velocity as seen in Figure 6(f), where the velocity is a function of size for both small and large droplets. Finally, it should be noted that as $t \to \infty$, all the droplets will eventually relax to the background gas velocity and the solution of the exact NDF relaxes to a monokinetic velocity distribution at $v = 0$ where U_x, Σ_{xx} and Σ_{xd} are zero, which is captured by the 20-moment AG closure.

5.3 Laminar Liquid Jet in a Crossflow at High Reynolds and Stokes Numbers

In the third test case, a liquid jet is injected into a crossflow with a Reynolds number of $Re = 8,636$. The problem is solved on a uniform planar mesh consisting of a total of 62,500 cells with eight cells across the jet inlet. The Haider-Levenspiel empirical correlation is used to specify C_D in this case. The Stokes number, which represents the ratio of the droplet relaxation time to the surrounding characteristic time scale, is very large for this case and as a result, there is a very high level of segregation of the droplet sizes, as can be seen in Figure 8(c). Due to the drag force, the spray evolves into "nearly-monodisperse" size distributions which occur when the moment vector approaches the boundary of realizability space and the distribution is defined as a linear combination of delta functions. Examples of the maximum-entropy solution can be seen in Figure 9, where it can be seen that in regions downstream of the jet, the size-conditioned number density is essentially a delta-function about $s = 0$ (blue curve). Consequently, maximum-entropy descriptions of these moment vectors can be challenging to obtain numerically since the optimization problem is poorly conditioned and distribution is very "peaked". However, it is promising that the proposed moment closure is capable of resolving the spray region where the segregation occurs as these situations are also expected in practical spray problems due to the segregating effects of drag forces.

(a) Total Droplet Number Density

(b) Mean Droplet x-velocity

(c) Mean Droplet Radius
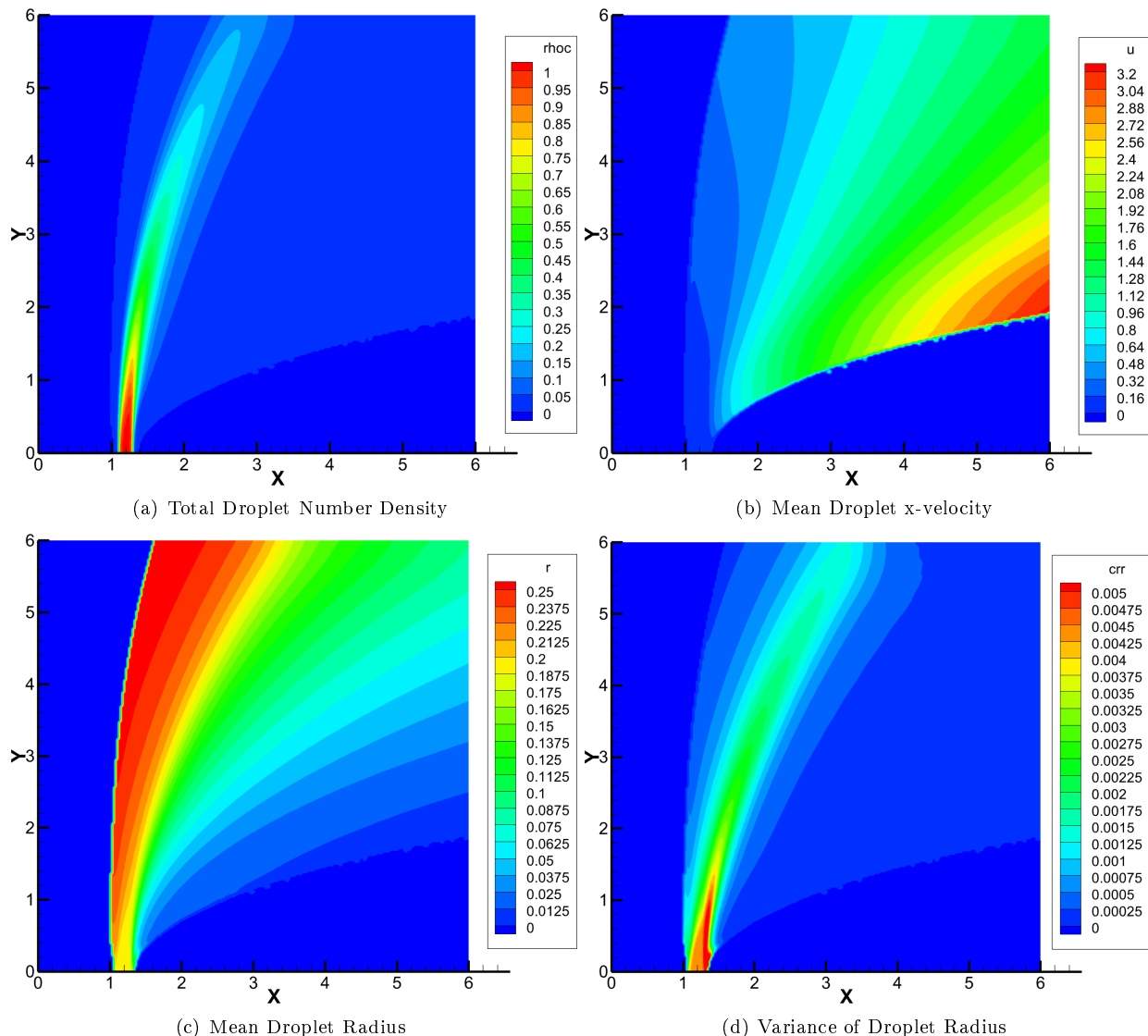

(d) Variance of Droplet Radius

Figure 8: Numerical predictions of the 20-moment AG closure a liquid jet in a crossflow showing the spatial distributions of various size and velocity moments.

5.4 Axisymmetric Turbulent Plain Orifice Atomizer

Finally, the EESA modelling approach outlined above is validated here using the conditions associated with the plain orifice atomizer of Wu *et. al* [31], which consists of a liquid water turbulent jet injected into a quiescent air environment. The Reynolds and Weber number of the liquid jet are $16,000$ and 94, respectively. The droplet drag coefficient in the disperse spray regime is modelled here again using the Haider-Levenspiel empirical correlation and turbulence in the carrier phase is modelled using the SST k-ω model [32]. The problem is solved on an axisymmetric mesh consisting of 500 cells ($800d$) in the axial direction, 50 cells in the radial direction ($250d$) and ten cells across the jet orifice, where d is the orifice diameter.

Contour plots for the predicted liquid mass fraction and mass-weighted surface density for the plain orifice atomizer are provided in Figures 10 and 11. The predictions of quasi-multiphase Σ-Y model alone are compared to those of the full EESA treatment. Finally, the droplet size distribution obtained from experiment after primary breakup is shown in Figure 12 and it can be seen that the predictions of the EESA moment approach is in rather good agreement with the predictions of the numerical model for the larger droplet sizes. However, as the EESA model results presented here do not include either droplet evaporation
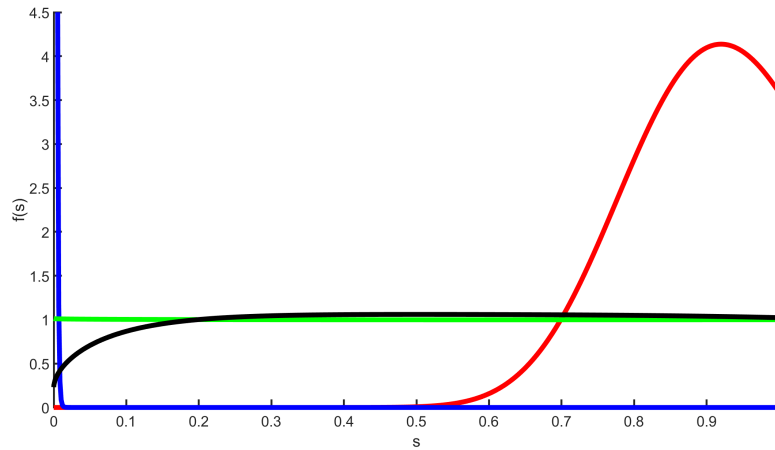
Figure 9: Predicted maximum entropy solutions of the size PDF, f(s), for liquid jet in a crossflow showing: (i) PDF at the inlet (green); (ii) PDF upstream of the jet (red); (iii) PDF at center of the jet (black); and (iv) PDF downstream of the jet (blue).
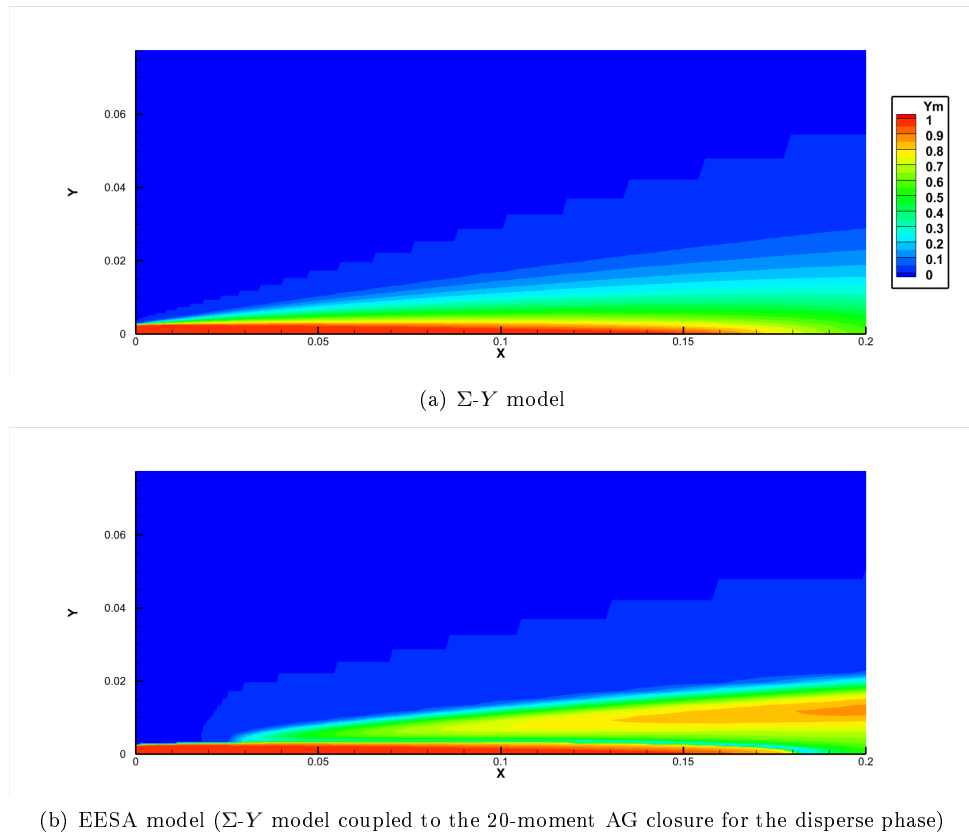

(a) Σ-Y model

(b) EESA model (Σ-Y model coupled to the 20-moment AG closure for the disperse phase)

Figure 10: Numerical predictions of the liquid mass fraction obtained for the plain orifice atomizer showing comparisons of the quasi-multiphase Σ-Y model to those of the EESA model based on the 20-moment AG closure for the disperse phase.

or secondary breakup, the smaller droplet sizes observed in experiment are not predicted in the simulation of the plain orifice atomizer. These effects will be examined in future studies.

(a) Σ-Y model

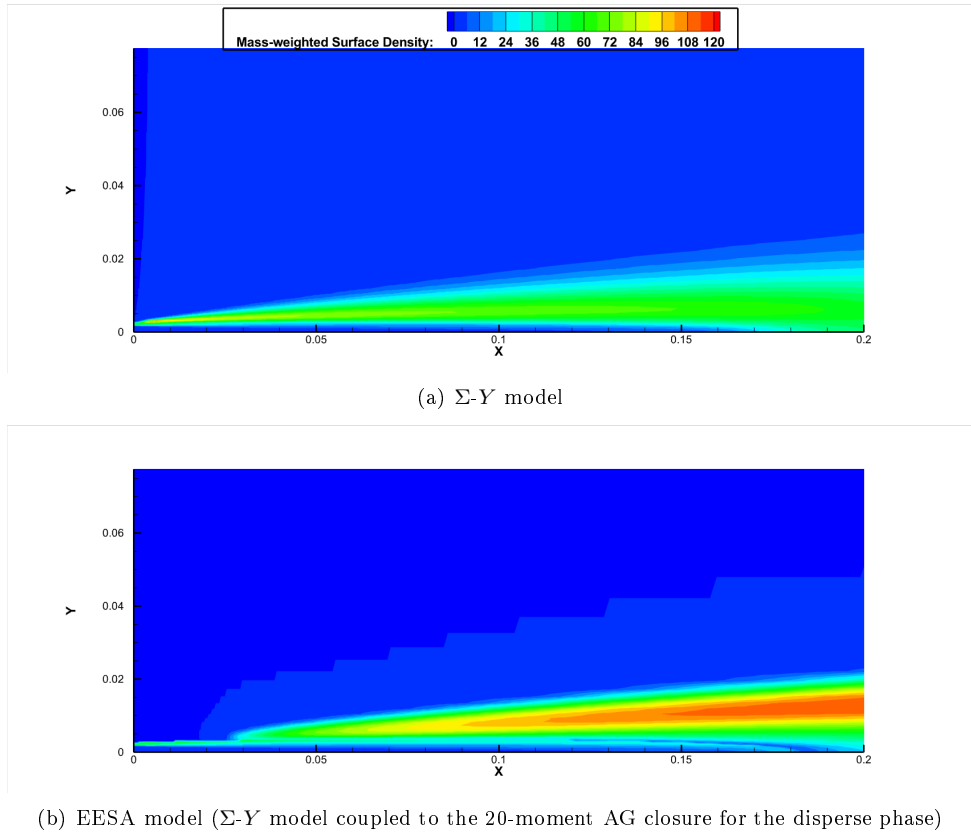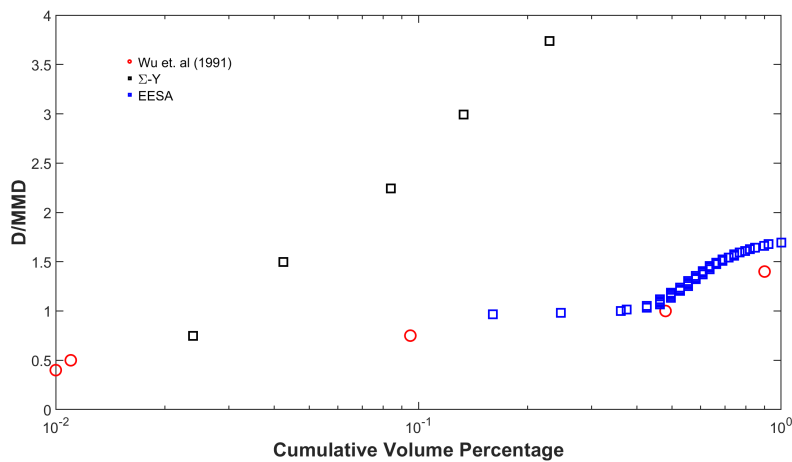(b) EESA model (Σ-Y model coupled to the 20-moment AG closure for the disperse phase)

Figure 11: Numerical predictions of the mass-weighted surface density obtained for the plain orifice atomizer showing comparisons of the quasi-multiphase Σ-Y model to those of the EESA model based on the 20-moment AG closure for the disperse phase.

Figure 12: Comparison of the predicted droplet size distribution after primary breakup obtained using the EESA model based on the 20-moment AG closure for the disperse phase to the experimental results of Wu *et. al* [31] for plain orifice atomizer.

6 Concluding Remarks

In this paper, a 20-moment polydisperse, polykinetic and Eulerian-based moment closure has been proposed based on the 10-moment AG closure for monodisperse sprays where modelling of the closing fluxes is achieved

using an interpolative approximation procedure and treatments for drag and evaporation are imposed though the use of source terms. The numerical framework is second-order and fully multi-dimensional with both one-way and two-way coupling to the gaseous background carrier phase. In addition, the proposed moment closure has been coupled with the Σ-Y model for a complete spray description of both dense and disperse spray regimes.

Several test cases are presented to demonstrate the predictive capabilities and robustness of the 20-moment AG closure under extreme conditions. Good agreement is shown when comparing the closure against the exact solution for a space-homogeneous problem and to the experimental results of a atomizing turbulent jet after primary breakup. In addition, the closure is tested for a laminar jet in crossflow with a very large Stokes number and is shown to be capable of handling spray regions where the size distribution is "nearly-monodisperse", which can naturally occur in practical problems involving drag but can be challenging for maximum-entropy-based moment closure methods to treat.

Future research will involve the validation of the proposed closure for a larger variety of practical spray configurations and comparison to solutions obtained using existing Lagrangian methods as well as available experimental data. The Eulerian framework of the 20-moment AG closure has many compelling advantages over a Lagrangian framework in terms of coupling to the background carrier phase and dense spray models since the solutions can be discretized using the same mesh. The eventual goal is to exploit the advantages of the Eulerian framework and show that solutions of comparable accuracy can be obtained at significantly reduced computational costs when Eulerian moment closure methods are used in place of more commonly adopted Lagrangian methods.

Acknowledgements

References

[1] L. Bayvel, Z. Orzechowski, Liquid Atomization, Taylor & Francis, Washington D.C., 1993.

[2] X. Gao, C. P. T. Groth, A parallel solution-adaptive method for three-dimensional turbulent non-premixed combusting flows, J. Comput. Phys. 229 (5) (2010) 3250–3275.

[3] X. Gao, S. A. Northrup, C. P. T. Groth, Parallel solution-adaptive method for two-dimensional non-premixed combusting flows, Prog. Comput. Fluid Dyn. 11 (2) (2011) 76–95.

[4] L. Freret, C. P. T. Groth, Anisotropic non-uniform block-based adaptive mesh refinement for three-dimensional inviscid and viscous flows, Paper 2015-2613, AIAA (June 2015).

[5] S. Subramaniam, Lagrangian-Eulerian methods for multiphase flows, Prog. Energy Combust. Sci. 39 (2013) 215–245.

[6] T. F. Leung, C. P. T. Groth, J. T. C. Hu, Evaluation of an Eulerian-Lagrangian spray atomization (ELSA) model for nozzle flow: Modeling of coupling between dense and disperse regions, Paper 2017-4352, AIAA (June 2017).

[7] P. Gualtieri, F. Picano, G. Sardina, C. M. Casciola, Exact regularized point particle method for multiphase flows in the two-way coupling regime, J. Fluid Mech. 773 (2015) 520–561.

[8] J. G. McDonald, C. P. T. Groth, Numerical modeling of micron-scale flows using the Gaussian moment closure, Paper 2005-5035, AIAA (June 2005).

[9] C. P. T. Groth, J. G. McDonald, Towards physically-realizable and hyperbolic moment closures for kinetic theory, Continuum Mech. Thermodyn. 21 (6) (2009) 467–493.

[10] C. K. S. Lam, C. P. T. Groth, Numerical prediction of three-dimensional non-equilibrium gaseous flows using the Gaussian moment closure, Paper 2011-3401, AIAA (June 2011).

[11] J. G. McDonald, J. S. Sachdev, C. P. T. Groth, Application of Gaussian moment closure to micro-scale flows with moving and embedded boundaries, AIAA J. 51 (9) (2014) 1839–1857.

[12] A. Vie, F. Doisneau, M. Massot, On the anisotropic Gaussian velocity closure for inertial-particle laden flows, Commun. Comput. Phys. 17 (2015) 1–46.

[13] F. A. Williams, Spray combustion and atomization, Phys. Fluids 1 (1958) 541–545.

[14] A. Wang, Eulerian-based moment methods for the modelling of polydisperse liquid sprays, Master's thesis, University of Toronto (October 2019).

[15] C. E. Shannon, A mathematical theory of communication, Bell System Technical Journal 27 (3) (1948) 379–423.

[16] E. T. Jaynes, Information theory and statistical mechanics, Physical Rev. 106 (1957) 620–630.

[17] A. Vié, F. Laurent, M. Massot, Size-velocity correlations in hybrid high order moment/multi-fluid methods for polydisperse evaporating sprays: Modeling and numerical issues, Journal of Computational Physics 237 (2013) 177 – 210.

[18] N. Agmon, Y. Alhassid, R. Levine, An algorithm for finding the distribution of maximal entropy, Journal of Computational Physics 30 (2) (1979) 250–258.

[19] L. R. Mead, N. Papanicolaou, Maximum entropy in the problem of moments, Journal of Mathematical Physics 25 (8) (1984) 2404–2417.

[20] G. W. Alldredge, C. D. Hauck, D. P. O'Leary, A. L. Tits, Adaptive change of basis in entropy-based moment closures for linear kinetic equations, J. Comput. Phys. 258 (2014) 489–508.

[21] D. Jones, A. Watkins, Droplet size and velocity distributions for spray modelling, Journal of Computational Physics 231 (2) (2012) 676–692.

[22] T. J. Stieltjes, Oeuvres complètes - Collected Papers, Vol. I & II, Springer-Verlag, Berlin, 1993.

[23] A. Haider, O. Levenspiel, Drag coefficient and terminal velocity of spherical and nonspherical particles, Powder Technology 58 (1) (1989) 63–70.

[24] A. Vallet, A. A. Burluka, R. Borghi, Development of an eulerian model for the "atomization" of a liquid jet, Atomization and Sprays 11 (6).

[25] R. Lebas, T. Menard, P. Beau, A. Berlemont, F. Demoulin, Numerical simulation of primary break-up and atomization: Dns and modelling study, International Journal of Multiphase Flow 35 (3) (2009) 247 – 260.

[26] P.-A. Beau, M. Funk, R. Lebas, F.-X. Demoulin, Applying quasi-multiphase model to simulate atomization processes in diesel engines: Modeling of the slip velocity, Tech. rep., SAE Technical Paper (2005).

[27] V. Venkatakrishnan, On the accuracy of limiters and convergence to steady state solutions, Paper 93-0880, AIAA (January 1993).

[28] A. Harten, P. D. Lax, B. van Leer, On upstream differencing and Godunov-type schemes for hyperbolic conservation laws, SIAM Rev. 25 (1) (1983) 35–61.

[29] C.-W. Shu, S. Osher, Efficient implementation of essentially non-oscillatory shock-capturing schemes, J. Comput. Phys. 77 (1988) 439–471.

[30] F. Forgues, L. Ivan, A. Trottier, J. G. McDonald, A gaussian moment method for polydisperse multiphase flow modelling, Journal of Computational Physics 398 (2019) 108839.

[31] P.-K. Wu, G. A. Ruff, G. M. Faeth, Primary breakup in liquid-gas mixing layers, in: 29th Aerospace Sciences Meeting, Aerospace Sciences Meetings, American Institute of Aeronautics and Astronautics, 1990.

[32] D. C. Wilcox, Turbulence Modeling for CFD, DCW Industries, La Cañada, 2002.